

# Sub- $2\mu\text{m}$ Gap Magnetic Flux Concentrators Coupled to Nano Spin Valve Sensors

Paulo Ricardo Veloso Coelho

paulo.coelho@tecnico.ulisboa.pt

*Under Supervision of Prof. Susana Cardoso Freitas and Prof. Diana Pinto Leitão*

INESC-MN, Lisboa, Portugal

Instituto Superior Técnico, Universidade de Lisboa, Lisboa, Portugal

September 2014

## Abstract

This work focus on the development of a high sensitivity magnetoresistive sensor with a sub- $100\mu\text{m}$  footprint towards high spatial resolution surface scanning applications. Nanometric spin valve sensors with synthetic ferrimagnet free layer centered in sub- $2\mu\text{m}$  gaps of magnetic flux concentrators were fabricated. Spin valves with synthetic antiferromagnet pinned layer and synthetic ferrimagnet free layer displayed sensitivities 2x (200 nm sensor) up to 4.5x (500 nm sensor) higher than simple top pinned or synthetic antiferromagnet spin valve structures. Magnetic flux concentrators with an area of  $100 \times 100 \mu\text{m}^2$  composed of a CoZrNb single layer were patterned by electron beam lithography and gap widths below  $2 \mu\text{m}$  were achieved. The magnetic and morphology profiles of the magnetic flux concentrators were characterized. 500 nm spin valves placed in the gap of the magnetic flux concentrators demonstrated sensitivities of  $\sim 0.37\%/\text{Oe}$  ( $1.8 \mu\text{m}$  gap) and  $\sim 0.46\%/\text{Oe}$  ( $1.65 \mu\text{m}$  gap) corresponding to maximum gains of 21x and 23x, respectively, when compared to isolated sensors. The average gain values experimentally obtained were in agreement with 3D FEM simulations performed. These devices may be incorporated in a XY scanning system to perform magnetic field mapping with a spatial resolution dependent on the device footprint.

**Keywords:** Magnetic Flux Concentrator, Nanometric Sensors, Sensitivity, Spin Valve, Synthetic Ferrimagnet

## 1. Introduction

Spin valve (SV) magnetoresistive (MR) sensors are extensively used nowadays for a wide range of sensing applications from recording/read heads [1] to magnetic imaging [2]. When combined with magnetic flux concentrators (MFCs), these sensors may

provide the desired features for room temperature detection of low magnetic fields below nanoTesla range [3][4]. Furthermore, particular applications, such as detection of magnetic single nanoparticles [5], also demand high spatial resolution, which in the case of magnetoresistive sensors is dependent

on their size. To fulfill such requirements one solution relies on the miniaturization of the magnetoresistive sensors down to sub-micrometric or nanometric dimensions, depending on the desired resolution. However, a reduction in the sensor size leads to a significant increase in the SVs demagnetizing effects. Most importantly, for linear SV sensors such decrease in size translates into higher saturation fields ( $H_{sat}$ ), which in turn lead to a decrease in sensitivity ( $S$ ) [6].

Therefore one can resort to engineered SV stacks where a synthetic-ferrimagnet (SF) free layer composed of ferromagnetic/spacer/ferromagnetic structure is used. In a SF the two ferromagnets are coupled (almost) antiferromagnetically through the thin spacer with a reduced effective magnetic thickness ( $t_{eff}$ ) [7] and effective saturation magnetization ( $M_{eff}^{SF}$ ). Since  $M_{eff}^{SF}$  is small, a decrease in the stray fields created by the free-layer occurs.  $H_{sat}$  is thus lowered and the sensors linear operation range can be tuned.

The main purpose of the MFCs is to increase the magnetic flux density within the gap where the sensor is placed. This increase is measured by a factor  $G$  which is the MFC gain, corresponding to the ratio of the effective magnetic field at the sensor region ( $H_{gap}$ ) and the external applied field ( $H_{external}$ ). Experimentally, the gain is obtained from the transfer curve of the MR sensor by comparing the field sensitivity  $S = \Delta\text{MR}/\Delta H$  of a device with MFC ( $S_w$ ) and the same sensor without MFC ( $S_{wo}$ ):

$$G = \frac{H_{gap}}{H_{external}} = \frac{S_w}{S_{wo}}. \quad (1)$$

In addition,  $G$  is also a geometric effect, and it increases linearly with the dimension of the flux concentrators, and decreases with the separation (*gap*) between MFCs,  $G \approx 1/gap$ .

In this work nanometric SV sensors with an optimized SF free layer and target heights below 500 nm

were fabricated. 3D simulations were performed to predict the gains obtained by the incorporation of MFCs. The materials used for the MFCs were optimized and their morphology and magnetics characterized. The gain in sensitivity of nano SV sensors in sub- $2\mu\text{m}$  gaps of MFCs was determined.

## 2. Experimental Details

All the SVs used in this work were deposited by ion beam deposition using a Nordiko 3000 system. The reference structure is a bottom pinned SV with a synthetic antiferromagnet (SAF) pinned layer and SF free layer with the following structure: Ta 20/ Ni<sub>80</sub>Fe<sub>20</sub> 30/ Mn<sub>75</sub>Ir<sub>25</sub> 80/ Co<sub>80</sub>Fe<sub>20</sub> 33/ Ru 8/ Co<sub>80</sub>Fe<sub>20</sub> 33/ Cu 25/ Co<sub>80</sub>Fe<sub>20</sub> 20/ Ni<sub>80</sub>Fe<sub>20</sub> 20/ Ru 12/ Ni<sub>80</sub>Fe<sub>20</sub> 25/ Ta 100 (thickness in Å and alloy composition in %). Unpatterned structures exhibited a magnetoresistance (MR) of 6.7 %, an offset field of  $H_o \approx 14$  Oe and a coercivity of  $H_c \approx 2$  Oe. The Ru thickness of the SF free-layer was optimized to ensure a smaller  $M_{eff}^{SF}$ . The sample were patterned into rectangular stripes by electron beam lithography (EBL) and ion milling etch with a length of  $l = 13\mu\text{m}$  and height ( $h$ ) ranging from 2  $\mu\text{m}$  down to 90 nm. In this case, and to decrease the effects of contact resistance as  $h$  decreases, triangular shaped ends were included to provide a larger area of contact with the SV.  $l$  was kept the longest possible (high aspect ratio  $l/h$ ) to ensure a well-defined magnetic behavior. The magnetizations of the pinned and free-layers were set orthogonally by shape anisotropy to provide a linear transfer curve. To provide a good electrical contact , with a critical alignment, a first set of contacts leads with a metallic layer of 400 Å Ru and 3000 Å AlSiCu protected with a 150 Å layer of TiWN<sub>2</sub> were defined by EBL and lift-off. Then the sensor was annealed for 15 min at 250 °C and cooled under an external magnetic field of 10 kOe to set the magnetization direction of the pinned layer.

The sensors were then incorporated in the gap

of two MFCs patterned by EBL. The electron beam resist consisted in a poly(methyl Methacrylate) (PMMA) tri-layer optimized to ensure an undercut profile for clean lift-off without residues and with a sufficiently high resolution  $\sim 1 \mu\text{m}$  in order to achieve gap widths below  $2 \mu\text{m}$ . A single layer of  $5000 \text{ \AA}$  of an amorphous alloy of  $\text{Co}_{93.5}\text{Zr}_{2.8}\text{Nb}_{3.7}$  (CZN) was deposited by DC Magnetron Sputtering with an uniaxial anisotropy parallel to the gap, induced by applying a magnetic field in plane. The concentrators were designed with an entrance width of  $100 \mu\text{m}$ , a pole width of  $2.5 \mu\text{m}$  and a total length of  $50 \mu\text{m}$ . Gaps down to  $\sim 1.65 \mu\text{m}$  were achieved (Fig.1(b)). A scanning electron microscope (SEM) image of the full device is exhibited in Fig.1(a).

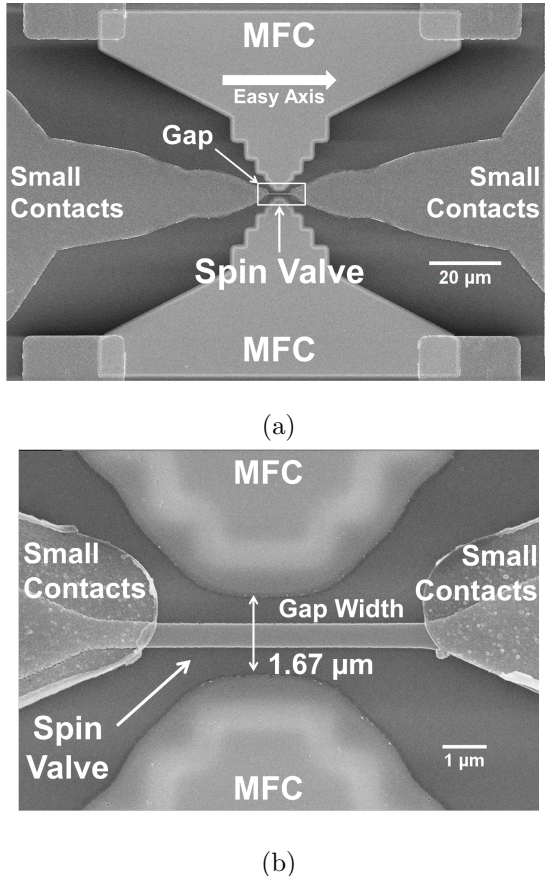


Figure 1: Top-view SEM images of (a) the entire device comprising the MFCs and the small electrical contacts to the sensor and (b) a detailed view of a  $500 \text{ nm}$  sensor in the smallest gap fabricated.

Scanning Electron Microscope (SEM) images were obtained with a Raith 150 system. The magnetic characterizations [M(H)] were performed by a KLA Tencor vibrating sample magnetometer (VSM) and the device's transfer curves were measured with a dc two-point probe method. Atomic/Magnetic Force Microscopy (AFM/MFM) measurements were performed in a Bruker Dimension Icon AFM at International Iberian Nanotechnology Laboratory (INL) and in a *Digital Instruments* Dimension 3000 AFM system at the Physics Department of Instituto Superior Técnico (IST).

### 3. Sensitivity Enhanced Spin Valves for Nanometric Sensors

In this section we studied the magnetic and magnetotransport properties of optimized SAF-SF SVs [8] in comparison to top-pinned and bottom pinned SAF SV structures, targeting applications within the nanoscale, where the demagnetizing effects usually dominate the magnetic properties. Figure 2(a) shows representative transfer curves for selected  $h$  of a bottom pinned SAF-SF SV. Overall a linear non-hysteretic behavior is observed for all sizes around  $H = 0$ . Also an increase in  $H_{\text{sat}}$  with decreasing  $h$  is clear due to freilayer's self-demagnetizing field ( $H_{\text{dem}}^{\text{FL}}$ ) enhancement for smaller sizes. In fact,  $H_{\text{sat}}$  can be approximated by  $H_{\text{dem}}^{\text{FL}}$ :

$$H_{\text{sat}} \approx H_{\text{dem}}^{\text{FL}} = 4\pi M_{\text{sat}}^{\text{FL}} \frac{t^{\text{FL}}}{h}, \quad (2)$$

where  $M_{\text{sat}}^{\text{FL}}$  is the saturation magnetization of the free layer and  $t^{\text{FL}}$  is the thickness of the ferromagnetic layers from the free layer. Figure 2(b) displays the  $\text{MR}(h)$  dependence, with a visible decrease in the MR value with decreasing  $h$ , being more notorious for  $h < 200 \text{ nm}$ . Such reduction can be firstly attributed to an increase in contact resistance ( $R_c$ ).  $R_c$  is defined as

$$R_c = R_{\text{low}} - \frac{l}{h} R_{\text{sheet}} - R_{\text{lead}}, \quad (3)$$

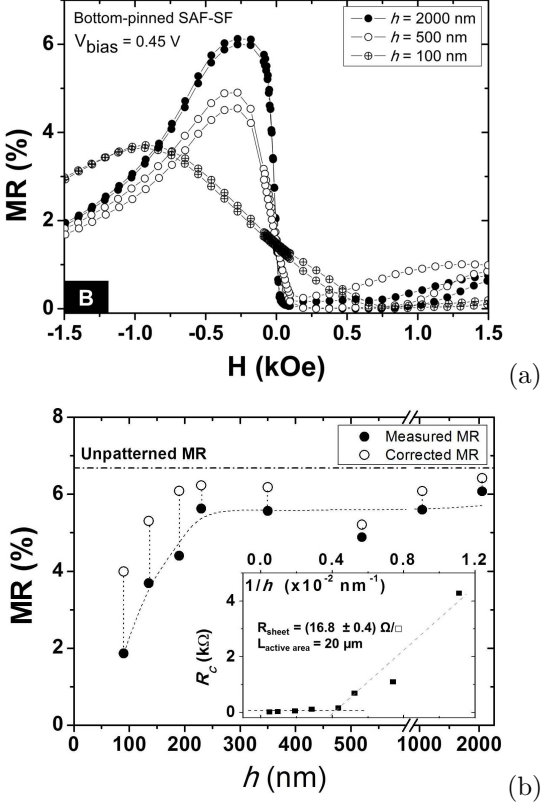


Figure 2: (a) Transfer curves of bottom-pinned SAF-SF SV for selected sizes ( $h$ ) measured with fixed  $V_{\text{bias}} = 0.45\text{ V}$ . (b) MR dependence on  $h$  for the bottom-pinned SAF-SF SV; the open dots correspond to the MR values obtained after removing the contribution from  $R_c$ . The inset shows the corresponding  $R_c$  dependence on  $1/h$

where  $R_{\text{low}}$  is the resistance of the SV in a parallel magnetization state,  $l$  the active length of the SV,  $R_{\text{sheet}}$  the sheet resistance of the sensor ( $\sim 17\Omega/\square$ ) measured by four-point probe method in unpatterned samples and  $R_{\text{lead}}$  the resistance of the electrical contacts ( $\sim 4\Omega$ ). Still, using  $R_c$  to calculate MR leads to a value close to the intrinsic one, except for  $h < 200\text{ nm}$ , where a considerable difference is still visible, not solely accounted by  $R_c$ . Similar results were obtained by Riedmüller *et al.*[9] in nanometric spin valves defined by focus ion beam. In fact, for lateral sizes smaller than 200 nm, previous works have reported a significant decrease in the exchange bias field [10] and weakened thermal stability due to edge roughness. Both effects can contribute to an overall reduction of the pinning

strength, which together with a significant increase in the local stray field effects as  $h$  decreases, may lead to deviations from fully crossed magnetic configuration between pinned (reference) and free layer magnetizations, translating into smaller MR. Moreover, an increase in  $H_o$  with  $h$  reduction was observed for all SVs. However, SAF-SF structures presented the lowest values for the same  $h$ . These results are mostly related to  $H_o$  dependence on  $1/t_{\text{eff}}$  of the free layer [7] (for a SAF-SF the free layer thickness is reduced from  $t_{\text{mag}} = 65\text{ \AA}$  to  $t_{\text{eff}} = 38\text{ \AA}$ ).

Figure 3(a) displays the impact of  $h$  in the sensor sensitivity, showing an overall decrease for smaller  $h$  values, consequence of larger  $H_{\text{sat}}$ . Also, and for  $h > 1000\text{ nm}$  the top-pinned SV exhibits a  $S(h)$  behavior similar to the SAF SV, being consistent with their identical free-layer structures. On the other hand, a major increase in  $S$  is observed for SAF-SF SVs, obtaining for  $h = 500\text{ nm}$  a  $S \approx 0.09\%/\text{Oe}$ , while  $S \approx 0.02\%/\text{Oe}$  for a corresponding SAF SV. Figure 3(b) summarizes the gain in sensitivity ( $S_{\text{SAF-SF}}/S_{\text{SAF}}$ ) achieved by employing SAF-SF when compared to SAF structures. The increase in  $S$  goes from 1.4 for  $h = 90\text{ nm}$  up to 4.5 for  $h = 500\text{ nm}$ . A dependence of the gain in  $h$  is clear, which is most probably related with the decrease in MR with size.

#### 4. 3D Simulations of Magnetic Flux Concentrators

A study of the MFCs gain as function of permeability (CZN and CoFeB/Ru SAF multilayers), shape, gap width and the inclusion of a spin valve sensor in the center of the gap was made using a finite element method software (COMSOL Multiphysics<sup>®</sup>). The 3D flux concentrators were designed in AutoCAD<sup>®</sup> and imported to COMSOL. First of all, an air box with dimensions  $155 \times 155 \times 20\mu\text{m}^3$  was created. A magnetic scalar potential ( $\psi_0$ ) of  $1.17\text{ A}$  was applied in one of the walls and a null potential on the wall across to gen-

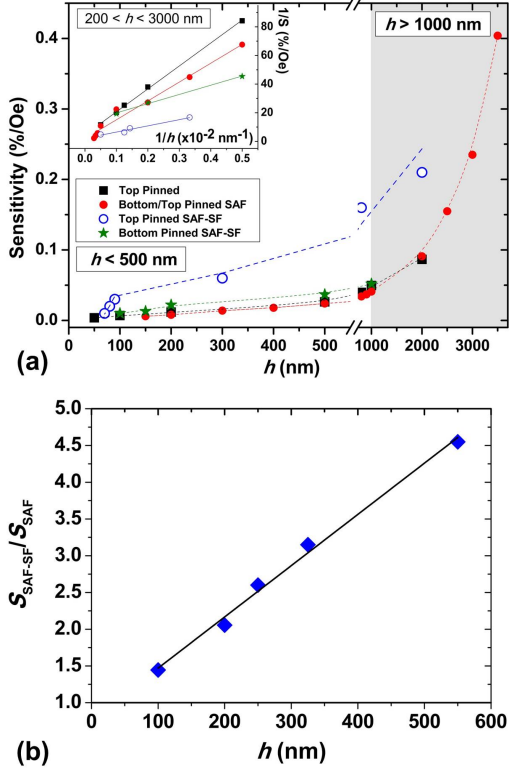


Figure 3: (a) Sensitivity dependence on  $h$  for different SVs. Inset shows the linear dependence of  $1/S$  with  $1/h$  for  $h > 200$  nm highlighting its expected linear dependence, where no significant decrease in MR occurs. (b) Gain in SV sensitivity for SAF-SF compared to a SAF highlighting sizes below 500 nm. Lines are a guide to the eye.

erate an homogeneous magnetic field of  $H = 95$  Oe, in the entire volume, according to  $H = -\nabla\psi$ . The impact of these parameters on the gain factor was investigated to assess which is the appropriate MFC geometry and to estimate and further compare with the gains of the fabricated devices. The gain was calculated according to Eq.1.  $H_{external} = 95$  Oe is the aforementioned homogeneous magnetic field inside the air box where the MFCs are placed. The  $H_{gap}$  was measured doing an average of the magnetic field in a rectangular area centered in the gap parallel to the poles.

A study was performed to five different MFC shapes. The gain in-gap was measured for two different types of materials, which possess different relative magnetic permeabilities ( $\mu_r$ ). The materi-

als chosen were a CZN single layer with a thickness of 3000 Å and CoFeB/Ru SAF multilayers (ML) (stack (Å): Ta 30/ Ru 20/ [CoFeB 50/ Ru 22]<sub>59</sub>/ CoFeB 50/ Ru 50) with a magnetic thickness (equivalent to the thickness of CoFeB layers) of 3000 Å. As CZN is magnetically softer it presents a higher unpatterned permeability,  $\mu_r = 715$  than the SAF multilayers,  $\mu_r = 82$ . The MFC dimensions are referred in section 2 and the gap width is 2 μm. Table 1 compiles the best results of the shape study. Shape 2 exhibits the higher gain factors.

Table 1: The three shapes with the highest gains for both CZN and CoFeB/Ru SAF ML

| Shape | Gain |        |
|-------|------|--------|
|       | CZN  | SAF ML |
| (1)   | 15.3 | 5.5    |
| (2)   | 18.3 | 8.2    |
| (3)   | 15.4 | 5.5    |

However, the exposure of this shape by EBL is not possible since the exposure conditions have not yet been optimized using the thick PMMA tri-layers. In addition, the magnetic domain structure at the pole may not be easily controlled causing a dipolar coupling between the poles and the sensor. Shapes 1 and 3 were selected for the next simulations and for fabrication. A study of the gap width on gain was also performed. The gap widths varied from 9 μm down to 1 μm. For both shapes and materials, it was observed a decreasing trend on gain with gap enlargement. The magnetic field in the gap follows the same trend,  $B \propto 1/r$ , in which  $r$  is the distance between the MFC pole and the center of the gap. In fact, the gain factor has the same proportionality relation with the gap  $G \propto 1/\text{gap} = 1/2r$ . Another part of the simulations consisted on spin valve-like elements with varying heights ( $h$ ) placed in the gap of the MFCs. This situation is a better approach to reality since in the experiments the

gain is measured by the ratio of sensitivities of the SVs with and without MFCs present. Nevertheless, the previously used relative permeabilities are for bulk materials and give rise to higher gains than in reality because  $\mu_r$  decreases for patterned elements [11]. Patterning films introduce additional shape anisotropy due to the demagnetization effects. The effective magnetic anisotropy ( $H_k^{eff}$ ) of patterned films is given by

$$H_k^{eff} = H_{ku} + 4\pi\epsilon M_{sat}, \quad (4)$$

where  $H_{ku}$  is the uniaxial anisotropy field of the unpatterned film,  $\epsilon$  is the demagnetization factor and  $4\pi M_{sat}$  is the saturation magnetization. For our calculations, we consider a demagnetization factor for an infinite stripe approximation,  $\epsilon = t/L$  for the MFC and  $\epsilon = t/h$  for the SV,  $t$  is the thickness of the film,  $L$  the length of the MFC and  $h$  the SV height. Magnetic permeability for patterned elements ( $\mu_p$ ) is given by [12]

$$\mu_p \approx 1 + \frac{\mu_b - 1}{1 + \epsilon(\mu_b - 1)}. \quad (5)$$

The patterned permeabilities are then  $\mu_p(\text{CZN}) \approx 93$  and  $\mu_p(\text{CoFeB/Ru SAF}) \approx 56$ . The gains for shape 3, both patterned materials, gap widths of 1  $\mu\text{m}$  and 2  $\mu\text{m}$  and with SV heights from 100 nm to 1000 nm are represented in Table 2.

Table 2: Gains obtained in the simulations for MFC with shape 3 and using  $\mu_p$  as magnetic permeability of the patterned structures.

| MFC                      | SV        | Gain |                    |
|--------------------------|-----------|------|--------------------|
| gap<br>( $\mu\text{m}$ ) | h<br>(nm) | CZN  | CoFeB/Ru<br>SAF ML |
| 2                        | no SV     | 7.9  | 5.9                |
|                          | 200       | 9.3  | 6.7                |
|                          | 500       | 10.4 | 7.5                |
|                          | 1000      | 14.1 | 10.1               |
| 1                        | no SV     | 14.5 | 10.3               |
|                          | 200       | 16.4 | 11.4               |
|                          | 300       | 17.7 | 12.4               |
|                          | 500       | 23.4 | 16.2               |

## 5. Final Device: SV Coupled to MFC

### 5.1. Magnetic Flux Concentrators

A method to obtain a linear and nonhysteretic enhanced magnetic field in the gap of the MFC consists in integrating, lamination similar, synthetic-antiferromagnetic (SAF) structures in which two ferromagnetic layers are separated by a thin non-magnetic spacer, providing a Ruderman-Kittel-Kasuya-Yosida (RKKY) long range interlayer antiferromagnetic (AFM) coupling between the two ferromagnets. In a multilayer configuration these SAF structures present a almost zero net remanent magnetic moment ( $M_r$ ) and the AFM coupling helps stabilizing the single domain state in each ferromagnetic layer [13]. (CoFeB/Ru)<sub>n</sub> multilayer thin films were prepared by IBD in a Nordiko 3600 system, from a target with a composition of (Co<sub>70</sub>Fe<sub>30</sub>)<sub>80at%</sub>B<sub>20at%</sub>. A Ru thickness of 22 Å and a CoFeB thickness of 50 Å were selected profiting from lower values of  $H_{sat}$  and a strong antiferromagnetic coupling between ferromagnetic layers translated by a low remanent magnetization normalized to saturation magnetization  $M_r/M_{sat} < 0.05$ . For MFC applications it is required that the product  $n \times t_F \times M_{sat} > 20 \text{ memu/cm}^2$  and  $H_{sat} < 50 \text{ Oe}$  [13] aiming higher relative magnetic permeabilities, therefore ML films with CoFeB layers need to have, at least, a magnetic thickness of 1700 Å. The deposited stack Ta 30Å/ Ru 20Å/(CoFeB 50/ Ru 22Å)<sub>59</sub>/ CoFeB 50Å/ Ru 50Å with n = 60 ferromagnetic layers ( $t_{mag} = 3000 \text{ \AA}$ ) presented the lowest value of  $M_r/M_{sat} \approx 0.016$ . Figure 4 exhibits the easy and hard axis of the optimized stack as well as some important magnetic properties. For a magnetic field applied along the easy axis the CoFeB layers exhibit a stable antiparallel magnetic state in the range of -20 Oe to 20 Oe and the hard axis curve exhibits a good linearity. The antiferromagnetic coupling field ( $H_{SAF} \sim 10^2 \text{ Oe}$ ) helps to minimize the effect of the internal demagnetizing fields

( $H_{\text{dem}} \sim 10^3$  Oe, at the MFC pole) arising from the size reduction of patterned structures, specially at the MFC poles.

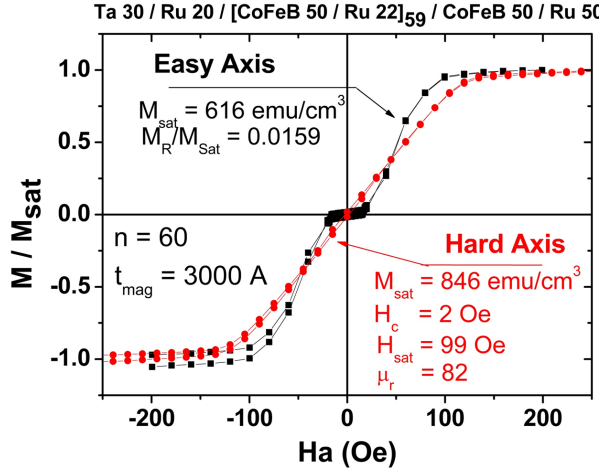


Figure 4: Easy and hard axis magnetic responses ( $M$ - $H$  loop) for SAF multilayers with  $n = 60$  CoFeB layers.

## 5.2. MFC Characterization: Morphology and Magnetics

A clean lift-off profile, with almost no residues, was observed in the vast majority of the inspected structures, as a result of the optimization of the PMMA tri-layer. However, in Fig.5 it is possible to observe that the vertexes of the rectangles are rounded and that only areas A2 and A3 are clearly distinguishable. The critical regions with features below  $2 \mu\text{m}$  are the poles areas A4 to A6 and the gap. The rounded features, particularly at the pole termination, may affect the magnetic domain arrangement in the area jeopardizing the MFC operation. A difference of about  $2 \mu\text{m}$  was found between nominal and measured sizes of the MFC. This reduction was attributed to the very small gap sizes, pushing the limits of the PMMA resolution thus enhancing the proximity effects.

Figures 6(a) and 6(b) show high resolution MFM scans performed over the MFCs pole (single structure) and centered on the MFCs gap (paired structures) in the remanent state. The MFCs were com-

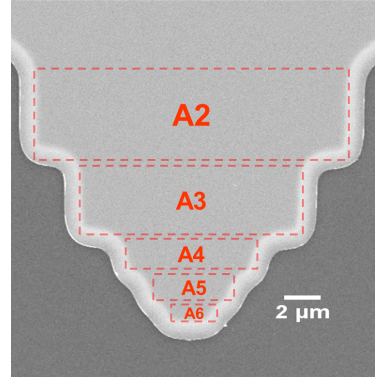


Figure 5: Gap and pole region of a MFC. Rectangles A2 to A6 represent, in descending order of size, different areas of the pole.

posed by a CZN single layer of 6000 Å. In both cases one observes the presence of closure domains (CDs). The orientation of the CDs is a consequence of the anisotropy induced during growth under an applied magnetic field, being reinforced by shape anisotropy. A good agreement is visible between measured and calculated domain sizes ( $d$ ). Deviations may occur due to stronger effects from shape anisotropy. Although the domain width at the termination of the poles is difficult to measure, the presence of closure domains in that region is essential to minimize dipolar coupling between MFCs. The MFC shape selection in section 4 envisaged this very purpose of the creation CDs at the pole. The particular geometry of the pole has two main advantages. The first is the squared geometry with sharp vertexes which are points of low anisotropy potentiating the formation of domains. The other advantage is the rectangular shape setting the direction of the shape anisotropy, arising from the demagnetizing effects, with the direction of the uniaxial anisotropy. The addition of the shape anisotropy reinforces the uniaxial anisotropy and prevents the rotation of the easy axis at pole.

## 5.3. Nano SV in sub- $2\mu\text{m}$ gap MFC

The devices studied in this part are composed of 500 nm SAF-SF SV sensors placed in sub- $2\mu\text{m}$  gaps

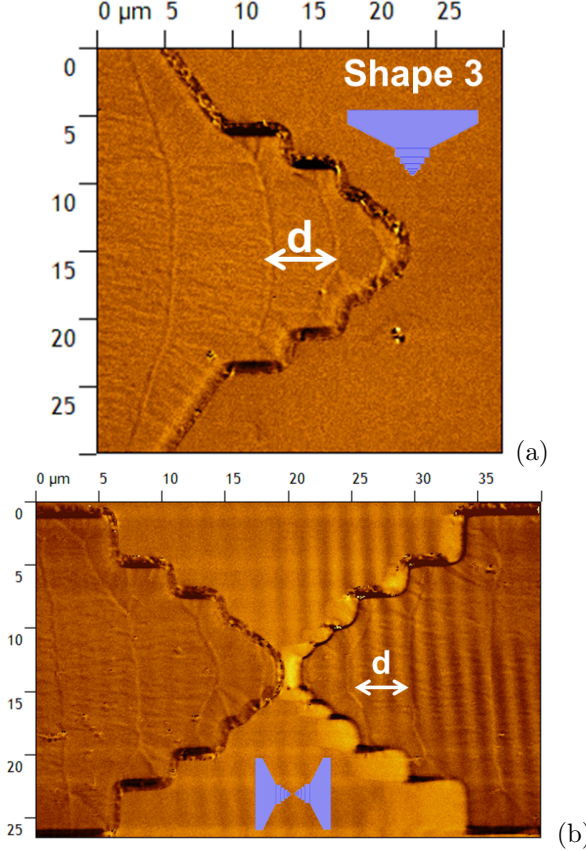


Figure 6: MFM images of shape 3 CZN MFCs corresponding to (a) a single structure (scan sweep of  $30 \mu\text{m}$ ) and (b) to a paired structure (scan sweep of  $40 \mu\text{m}$ ). d corresponds to the domain width.

of two patterned magnetic flux concentrators composed of CZN with a nominal thickness of  $5000 \text{ \AA}$ , to study the enhancement in sensitivity produced in the sensor by its inclusion in such small gaps.

Figure 7 shows the M-H loop for the unpatterned CZN film. According to Eq.5 after patterning the MFC  $\mu_r$  decreases to  $\mu_p \approx 96$ .

MFCs with gap widths of  $\sim 1.8 \mu\text{m}$  and  $\sim 1.65 \mu\text{m}$  were achieved. Figures 8(a) and 8(b) show the transfer curves [MR(H)] of SV sensors in two different gap widths of MFCs and their corresponding isolated sensor (measured prior to MFC definition). The selected curves display the maximum gain ( $G_{\max}$ ) obtained. The gain is determined through the ratio between the sensitivity of the sensor with and without MFC (Eq. 1). For the MFC with a gap  $\approx 1.8 \mu\text{m}$ , a  $G_{\max} = 21.3$  was obtained,

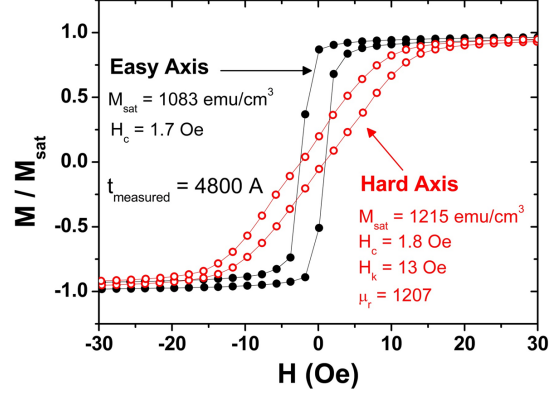


Figure 7: Easy and hard axes M-H loop obtained for an unpatterned sample of the CZN film deposited.

with an average gain of 16.8 from a total of 18 measured devices. The sensitivity improved from 0.017 %/Oe to a maximum of 0.370 %/Oe. For the MFC with a gap  $\approx 1.65 \mu\text{m}$ , a  $G_{\max} = 23.4$  was obtained, with an average gain of 17.4 from a total of 16 measured devices. The sensitivity improved from 0.020 %/Oe to a maximum of 0.460 %/Oe. It was also observed, among all the structures measured, a decrease in the offset field  $H_o$  from  $\sim 70$  Oe in the isolated sensor to  $\sim 4$  Oe. Despite the small increase in  $H_c$  of the sensor after the incorporation of MFCs reported in previous works [4], in our case there was no change in coercivity with the inclusion of the flux concentrators.

Figure 9 compares the gains in sensitivity obtained experimentally with the ones obtained by FEM simulations of patterned MFCs with a 500 nm SV-like sensor in gap (see Table 2). The error bars of the average gains correspond to the standard deviations. For devices with gaps of  $1.8 \mu\text{m}$  and  $1.65 \mu\text{m}$  the average gains are very close to the ones obtained by simulation. The slightly higher gains demonstrated by the fabricated devices may be due to the fact of not accounting for the  $75^\circ$  tapered profile MFC in the gap achieved experimentally in the simulations where only steep profile MFCs were used.

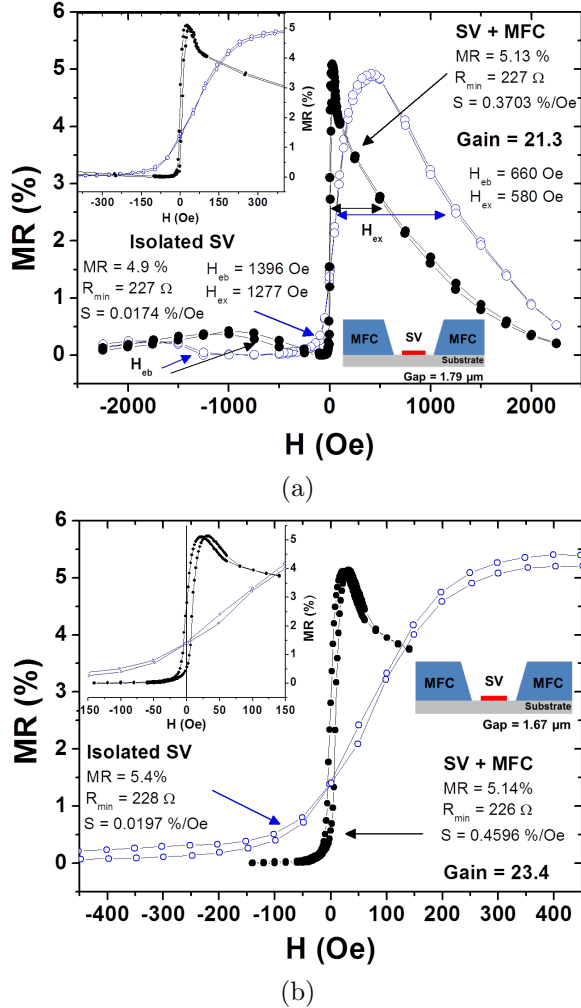


Figure 8: Transfer curves ( $I_{\text{bias}} = 100 \mu\text{A}$ ) for the devices with MFC gap widths of (a)  $1.79 \mu\text{m}$  and (b)  $1.67 \mu\text{m}$  exhibiting the maximum gain achieved.

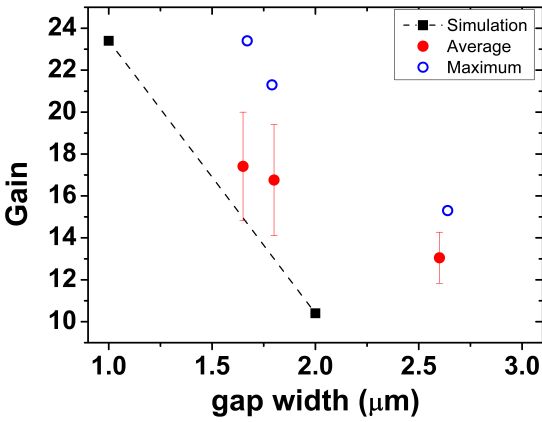


Figure 9: Comparison between the experimental gains in sensitivity with the ones obtained via 3D simulations of MFC with a  $h = 500 \text{ nm}$  SV-like stripe element centered in the gap.

## 6. Conclusions

This work aimed the development of a high sensitivity device with a reduced footprint towards high resolution and low field detection applications, namely magnetic field mapping. To fulfill these requirements the following structures were fabricated: (i) magnetic flux concentrators with a reduced area ( $100 \times 100 \mu\text{m}^2$ ) and sub- $2\mu\text{m}$  gap and (ii) nanometric spin valve sensors with synthetic ferrimagnet free layer and target heights below 500 nm to fit in the sub- $2\mu\text{m}$  gap of the magnetic flux concentrators.

The magnetic properties of top-pinned, bottom-pinned SAF and bottom/top-pinned SAF-SF nanometric sized SVs were studied. SAF-SF SVs displayed the highest values in sensitivity, namely for the target sizes below 500 nm. Gains in sensitivity from  $\sim 1.4$  ( $h = 90 \text{ nm}$ ) up to  $\sim 4.5$  ( $h = 500 \text{ nm}$ ) were obtained for SAF-SF SVs in comparison to bottom-pinned SAF and top-pinned SVs. The use of SAF-SF structures helped to minimize the losses in sensor sensitivity when patterning SVs with nanometric lateral sizes ( $h < 500 \text{ nm}$ ). The incorporation of these synthetic structures in SVs stands as a strategy to achieve competitive nanoscale sensors with high sensitivity and high spatial resolution. 3D simulation of magnetic flux concentrators were performed using FEM software in order to study the effects of shape, gap width and inclusion of a spin valve-like element in the gap of MFCs in the amplification of the magnetic field in gap. For a  $1 \mu\text{m}$  gap, the obtained gains were  $G$  (CZN)  $\sim 15$  and  $G$  (CoFeB/Ru SAF)  $\sim 11$  with a  $100 \text{ nm}$  SV in gap up to  $G$  (CZN)  $\sim 23$  and  $G$  (CoFeB/Ru SAF)  $\sim 16$  with  $500 \text{ nm}$  SV in gap. The nanometric SV sensors ( $h = 500 \text{ nm}$ ) response with and without CZN single-layer MFCs was studied. Maximum gains in sensitivity of 21.3 and 23.4 were achieved for devices in between MFCs with gap widths of  $\sim 1.8 \mu\text{m}$  and  $\sim 1.65 \mu\text{m}$ , respectively. The average gain values were in agreement with 3D FEM simulations performed.

Further work must be done to fully characterize the device and some modifications may be attempted to optimize the device envisaging its integration in an automatic magnetic field scanning/imaging system.

## References

- [1] M. Carey, S. Maat, S. Chandrashekariaih, J. Katine, W. Chen, B. York, and J. Childress, “Co<sub>2</sub>MnGe-based current-perpendicular-to-the-plane giant-magnetoresistance spin-valve sensors for recording head applications,” *Journal of Applied Physics*, vol. 109, no. 9, p. 093912, 2011.
- [2] M. Pannetier-Lecoeur, L. Parkkonen, N. Sergeeva-Chollet, H. Polovy, C. Fermon, and C. Fowley, “Magnetocardiography with sensors based on giant magnetoresistance,” *Applied Physics Letters*, vol. 98, no. 15, 2011.
- [3] A. Guedes, J. Almeida, S. Cardoso, R. Ferreira, and P. Freitas, “Improving magnetic field detection limits of spin valve sensors using magnetic flux guide concentrators,” *Magnetics, IEEE Transactions on*, vol. 43, no. 6, pp. 2376–2378, 2007.
- [4] D. C. Leitao, L. Gameiro, A. V. Silva, S. Cardoso, and P. P. Freitas, “Field detection in spin valve sensors using CoFeB/Ru synthetic antiferromagnetic multilayers as magnetic flux concentrators,” *Magnetics, IEEE Transactions on*, vol. 48, no. 11, pp. 3847–3850, 2012.
- [5] R. S. Gaster, L. Xu, S.-J. Han, R. J. Wilson, D. A. Hall, S. J. Osterfeld, H. Yu, and S. X. Wang, “Quantification of protein interactions and solution transport using high-density gmr sensor arrays,” *Nature nanotechnology*, vol. 6, no. 5, pp. 314–320, 2011.
- [6] P. Freitas, R. Ferreira, S. Cardoso, and F. Cardoso, “Magnetoresistive sensors,” *Journal of Physics: Condensed Matter*, vol. 19, no. 16, p. 165221, 2007.
- [7] A. Veloso and P. P. Freitas, “Spin valve sensors with synthetic free and pinned layers,” *Journal of Applied Physics*, vol. 87, no. 9, 2000.
- [8] P. Coelho, D. Leitao, J. Antunes, S. Cardoso, and P. Freitas, “Spin valve devices with synthetic-ferrimagnet free-layer displaying enhanced sensitivity for nanometric sensors,” *Magnetics, IEEE Transactions on*, 2014 (to be published).
- [9] B. Riedmüller, F. Huber, and U. Herr, “Towards sub-200 nm nano-structuring of linear giant magneto-resistive spin valves by a direct focused ion beam milling process,” *Journal of Applied Physics*, vol. 115, no. 6, p. 064307, 2014.
- [10] V. Baltz, J. Sort, S. Landis, B. Rodmacq, and B. Dieny, “Tailoring size effects on the exchange bias in ferromagnetic-antiferromagnetic 100 nm nanostructures,” *Physical review letters*, vol. 94, no. 11, p. 117201, 2005.
- [11] X. Chen, Y. Ma, and C. Ong, “Magnetic anisotropy and resonance frequency of patterned soft magnetic strips,” *Journal of Applied Physics*, vol. 104, no. 1, p. 013921, 2008.
- [12] G. Perrin, J. Peuzin, and O. Acher, “Control of the resonance frequency of soft ferromagnetic amorphous thin films by strip patterning,” *Journal of applied physics*, vol. 81, no. 8, pp. 5166–5168, 1997.
- [13] I. Trindade, J. Oliveira, R. Fermento, J. Sousa, S. Cardoso, P. P. Freitas, A. Raghunathan, and J. Snyder, “Soft thin films for flux concentrators,” *Magnetics, IEEE Transactions on*, vol. 45, no. 1, pp. 168–171, Jan 2009.